Polyhedron 262 (2024) 117162

Contents lists available at ScienceDirect

Polyhedron

journal homepage: www.elsevier.com/locate/poly

Structural insights and photophysical properties of mononuclear and pentanuclear Zn(II) acetate complexes with pyridyl-based thiazolyl-hydrazones

Jovana B. Araškov [a], Alfonso T. Garcia-Sosa [b,*], Aleksandar Višnjevac [c], Sérgio F. Sousa [d,e], Berta Barta Holló [f], Özlem Uğuz [g], Atıf Koca [g], Miguel Monge [h], María Rodríguez-Castillo [h], José M. López-de-Luzuriaga [h], Tamara R. Todorović [a], Nenad R. Filipović [i,*]

[a] University of Belgrade – Faculty of Chemistry, Studentski trg 12-16, 11000 Belgrade, Serbia
[b] Institute of Chemistry, University of Tartu, Ülikooli 18, 50090 Tartu, Estonia
[c] Division of Physical Chemistry, Institute Ruđer Bošković, Bijenička cesta 54, 10000 Zagreb, Croatia
[d] UCIBIO – Applied Molecular Biosciences Unit, BioSIM – Department of Biomedicine, Faculty of Medicine, University of Porto, 4200-319 Porto, Portugal
[e] Associate Laboratory i4HB – Institute for Health and Bioeconomy, Faculty of Medicine, University of Porto, 4200-319 Porto, Portugal
[f] University of Novi Sad, Faculty of Sciences, Trg Dositeja Obradovića 4, 21000 Novi Sad, Serbia
[g] Marmara University, Engineering Faculty, Department of Chemical Engineering, 34722 Goztepe, Istanbul, Turkey
[h] Departamento de Química, Instituto de Investigación en Química de la Universidad de La Rioja (IQUR), Universidad de La rioja. Complejo Científico-Tecnológico, 26006 Logroño, Spain
[i] University of Belgrade – Faculty of Agriculture, Nemanjina 6, 11000 Belgrade, Serbia

ARTICLE INFO

Keywords:
Zn(II) complexes
Intermolecular interactions
Thiazolyl-hydrazones
Photoluminescence
TD-DFT

ABSTRACT

The solid state structures of zinc complexes with HLS^1 and HLS^3 ligands are reported, where HLS^1 is 2-(2-(pyridin-2-ylmethylene)hydrazinyl)-4-fenil-1,3-thiazole and HLS^3 is 2-(2-(pyridin-2-ylmethylene)hydrazinyl)-4-(4-methylphenyl)-1,3-thiazole. Structurally similar ligands form complexes of different structures with general formulas $[Zn_5(LS^1)_4(AcO)_6]$ (**1-AcO**) and $[Zn(LS^3)(AcO)(H_2O)]$ (**3-AcO**). The pentacoordinated complex **3-AcO** exhibits *NNN* tridentate ligand coordination mode, with additional oxygen donor atoms from a water molecule and acetate anion. The structure of **1-AcO** is unique as it is the first example of a pentanuclear complex with pyridyl-based thiazolyl-hydrazone ligands, containing an unprecedented centrosymmetric $Zn_3(AcO)_6$ cluster. Photophysical studies showed that **1-AcO** is not photoactive, while **3-AcO** displayed photoluminescent emission, attributed to ligand-based transitions as determined by time-dependent density functional theory (TD-DFT) calculations. This study underscores the role of molecular symmetry in predicting the photoactivity of at least Zn (II) complexes containing photo-inactive ligands.

1. Introduction

Pyridine-based thiazolyl-hydrazones (PTHs, Scheme 1) contain a hydrazone bridge between pyridine and 1,3-thiazole rings. They can be easily obtained by the Hantzsch reaction of pyridyl-thiosemicarbazones and α-bromoketones (Scheme 1). These compounds possess one sulfur and four nitrogen donor atoms. Additional donor atoms in PTHs can be introduced using suitable α-bromoketones that determine R4 substituent. Currently, two PTH classes of ligands have been studied: I-class containing one pyridine ring and II-class with an additional pyridine ring (R4 substituent, Scheme 1). One line of the research in our group is devoted to *d*-metal complexes with I-class PTH ligands ($HLS^{1–3}$; Scheme 1). Single crystal X-ray diffraction (XRD) data indicate *NNN* tridentate coordination of $HLS^{1–3}$, with the involvement of pyridine, imine, and thiazole nitrogen atoms, in mononuclear Co(III), Zn(II), and Cd(II) complexes that have been the subject of our studies up to now [1–6]. The same coordination mode was noticed in mononuclear Co(III), Zn(II), and Ni(II) complexes with related L^1 and L^2 ligands (Scheme 1), published by Bera et al. [7–9]. On the other hand, ligands L^3–L^6 from the second class (Scheme 1), designed by Li et al., form mononuclear and polymeric complexes with *d*-metals [10–13]. Analysis of single crystal XRD data indicates different coordination modes of L^3–L^6, whereby the pyridine

* Corresponding authors.
E-mail addresses: t.alfonso@gmail.com (A.T. Garcia-Sosa), nenadf@agrif.bg.ac.rs (N.R. Filipović).

https://doi.org/10.1016/j.poly.2024.117162
Received 19 June 2024; Accepted 26 July 2024
Available online 27 July 2024

nitrogen atom (R4 substituent, Scheme 1) is coordinated in all Ni, Zn, and Cd complexes.

Zinc is a *d*-metal with a d^{10} electronic configuration and a zero crystal field stabilization energy value. Thus, there is no preference for its complexes' specific geometries and coordination numbers (CNs). The most frequent geometries for zinc are octahedral, tetrahedral, and square-pyramidal, but other geometries are also known. On the other hand, its CNs range from 2 to 9 (most often 4–6) [14]. Both geometries and CNs are influenced by steric and electronic factors of ligands, as well as by the nature of anions originating from zinc salts used to synthesize its complexes. The growing interest in zinc complexes can be attributed to their interesting coordination chemistry and the fact that zinc is less toxic and cheaper than most metals. As an illustration of the above-mentioned, we point out the comparative analysis of PubMed data regarding the number of studies devoted to zinc and other *d*-metal complexes in 2019–2023 (Table S1, Electronic Supplementary Information, ESI). The analysis reveals that zinc complexes are the fourth most studied *d*-metals complexes. They have been studied regarding the application based on their anticancer [15,16], antifungal [17], antibacterial [18–23], antiviral [24–27], antidiabetic [28], and bioimaging properties [29]. Zinc complexes were also studied because of their catalytic [30–32], and optical properties [33–38]. The latter is particularly important since the exciting development of solid-state emitters has been the focus of extensive research to create new materials for unconventional uses, such as organic light-emitting diodes (OLEDs), photodetectors, data storage, and solar cells [39]. Organic solid emitters offer several benefits, including low density, the ability to be processed in solution, vast design possibilities, and easy fabrication without significant environmental impact. The recent review summarizes the latest advancements in solid-state emissive organic crystals and co-crystals [39]. In developing affordable solid-state lighting devices, exploring new emitters derived from readily available, cost-effective, and non-toxic metal complexes is essential [40,41]. In this pursuit, Zn(II) complexes have emerged as a promising substitute for the costly transition metal complexes utilizing iridium, platinum, or osmium [40,41]. In addition, excited states with metal-to-ligand charge transfer (MLCT) properties are particularly preferred for d^{10} transition metal complexes due to the occupation of all d orbitals, which suppresses non-radiative d → d* electronic transitions, also known as metal-centered electronic transitions (MC). This specific electronic configuration of the d^{10} metal center clarifies the substantial focus on Zn(II) complexes, in addition to other d^{10} metal complexes, for solid-state lighting applications [41].

Previously, we have reported the structures of nine Zn(II) complexes with HLS^{1-3} ligands, synthesized under the same experimental conditions, starting from different zinc salts (chloride, nitrate, perchlorate, and acetate; Table 1) [5,6].

We have studied the complexes as multifunctional materials regarding their applications as anticancer agents and electrochromic and photoactive materials [5,6]. The complexation of HLS^{1-3} with Zn(II) resulted in the corresponding complexes' with more potent anticancer

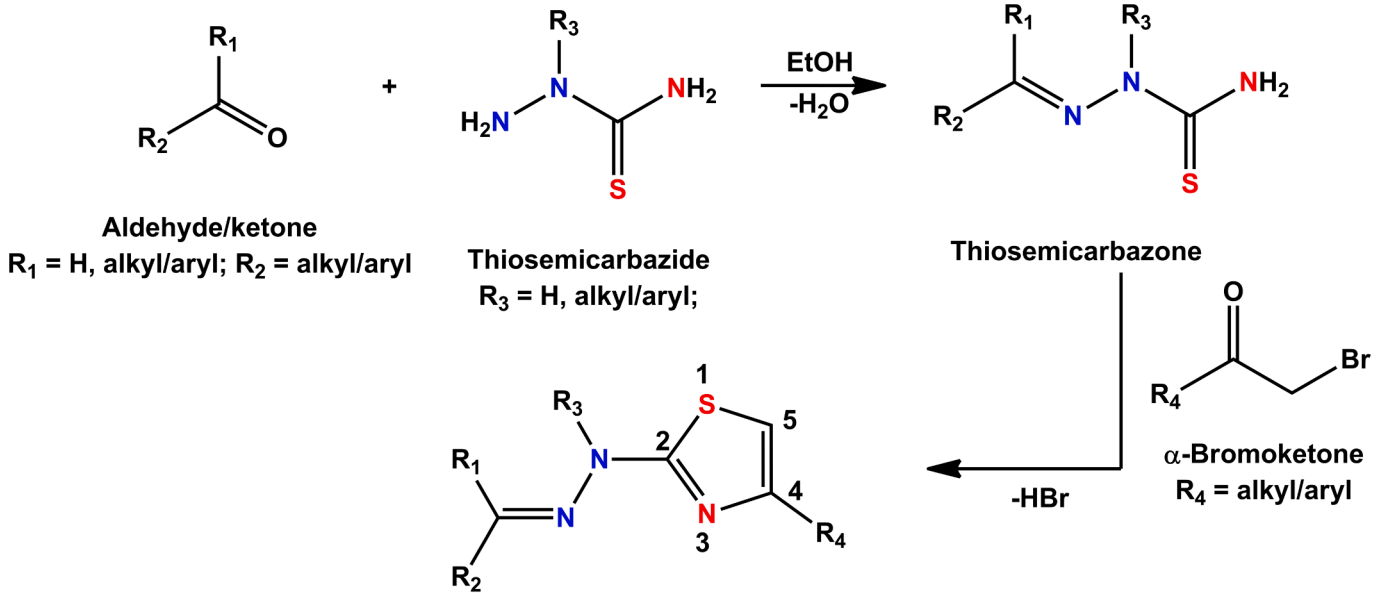

Pyridine based thiazolyl-hydrazone (PTHs)

I class PTH ligands

Label	R_1	R_2	R_3	R_4
HLS^1	2-Pyridine	H	H	Ph
HLS^2	2-Pyridine	H	H	PhOMe
HLS^3	2-Pyridine	H	H	PhMe
L^1	2-Pyridine	Me	H	PhOMe
L^2	2-Pyridine	Ph	H	PhCN

II class PTH ligands

Label	R_1	R_2	R_3	R_4
L^3	2-Pyridine	H	H	2-Pyridine
L^4	3-Pyridine	H	H	3-Pyridine
L^5	4-Pyridine	H	H	3-Pyridine
L^6	4-Pyridine	H	H	2-Pyridine

Scheme 1. Pyridine-based thiazolyl-hydrazones (PTHs): preparation and examples.

Table 1
Zn complexes with HLS^{1-3} studied in our group.

Ligands	Chloride-based complexes		Nitrate-based complexes		Neutral complexes	
	Formula	Label	Formula	Label	Formula	Label
HLS^1	$[Zn(HLS^1)Cl_2]$	**1-Cl**	$[Zn(HLS^1)_2](NO_3)_2{\cdot}H_2O$	**1-NO_3**	$[Zn(LS^1)_2]$	**1**
HLS^2	$[Zn(HLS^2)_2][ZnCl_4]$	**2-Cl**	$[Zn(HLS^2)_2](NO_3)_2{\cdot}H_2O{\cdot}MeOH$	**2-NO_3**	$[Zn(LS^2)_2]$	**2**
HLS^3	$[Zn(HLS^2)_2][ZnCl_4]$	**3-Cl**	$[Zn(HLS^3)_2](NO_3)_2{\cdot}0.5DMF$	**3-NO_3**	$[Zn(LS^3)_2]$	**3**

activity than the parent ligands. Spectral changes observed during the first reduction and oxidation processes of **1** resulted in distinct spectral color changes, indicating the possible functionality of this type of Zn complexes for electrochromic applications [5,6]. Photophysical studies showed that the complexation of photophysically non-active HLS^{1-3} ligands with Zn(II) ion induced photoluminescent properties, but only in asymmetrical complexes (**1-Cl**, **1–3-NO_3**, **1–3**, Table 1) [5,6]. This observation was very interesting since photoactive complexes **2-NO_3/3-NO_3** share the same complex cation as their non- photoactive symmetrical chloride counterparts **2-Cl/3-Cl** with Zn(II) ions situated at two-fold axis [5,6]. Detailed structural analysis of chemically identical complex cation pairs **2-NO_3/2-Cl** and **3-NO_3/3-Cl** indicated significant differences in the conformation of their pyridine and benzene rings. These differences originated from different distribution of intermolecular interactions. In the case of **2-Cl/3-Cl**, the most prominent intermolecular contacts appeared to be H···Cl. In contrast, for **2-NO_3/3-NO_3**, the main intermolecular contacts are H···O. To further evaluate the role of asymmetry of zinc complexes with non-photoactive ligands as a cause of photoluminescent activity, we have also performed a Cambridge Structural Database search to identify all symmetrical zinc complexes for which photoactivity in the solid state was studied. The search confirmed our observation regarding zinc complexes with HLS^{1-3} ligands. Therefore, we hypothesized that a photoactivity of complexes in the solid state, in which the Zn(II) ions lie on a symmetry element, would be manifested only if the corresponding ligand exibits pre-existing photophysical properties [5].

In the synthesized series of Zn(II) complexes (Table 1), all complexes are octahedral except **1-Cl**, which has a trigonal–bipyramidal geometry around the Zn(II) ion. The complexes **1–3** contain in the inner sphere the ligands coordinated in anionic form since KOH (in the case of **1**) or acetate ions (**2** and **3**) served as a base for the ligand deprotonation [6]. However, it is well known that acetate ion can be coordinated as monodentate and chelate ligand, as well as *via* various bridging modes [14]. The coordination preferences of acetate ion to Zn(II) were revealed by a CSD analysis (Scheme 2) [14]. In cca. 97 % of the structures found in the CSD, the acetates are bonded to Zn(II). Monodentate coordination mode ($\eta^1{:}\eta^0$, Scheme 2) is the most common one. Among all bridging coordination modes, a bidentate bridging mode ($\mu_2{-}\eta^1{:}\eta^1$) is the most common, while a chelate bridging mode ($\mu_2{-}\eta^2{:}\eta^1$) is one of the least represented (Scheme 2). Interestingly, to the best of our knowledge there are no strucures of Zn(II) complexes with PTH ligands with simultaneously coordinated acetate ion(s) deposited in the CSD [14].

Considering all the above, the primary goal of the present study was to obtain the first acetate-based zinc complexes with PTH ligands and study the impact of acetate ion coordination on their solid-state structures. The second goal was to determine the photophysical properties of these novel complexes and further test our hypothesis on the cause of solid-state photoluminescence of Zn(II) complexes with photo-inactive

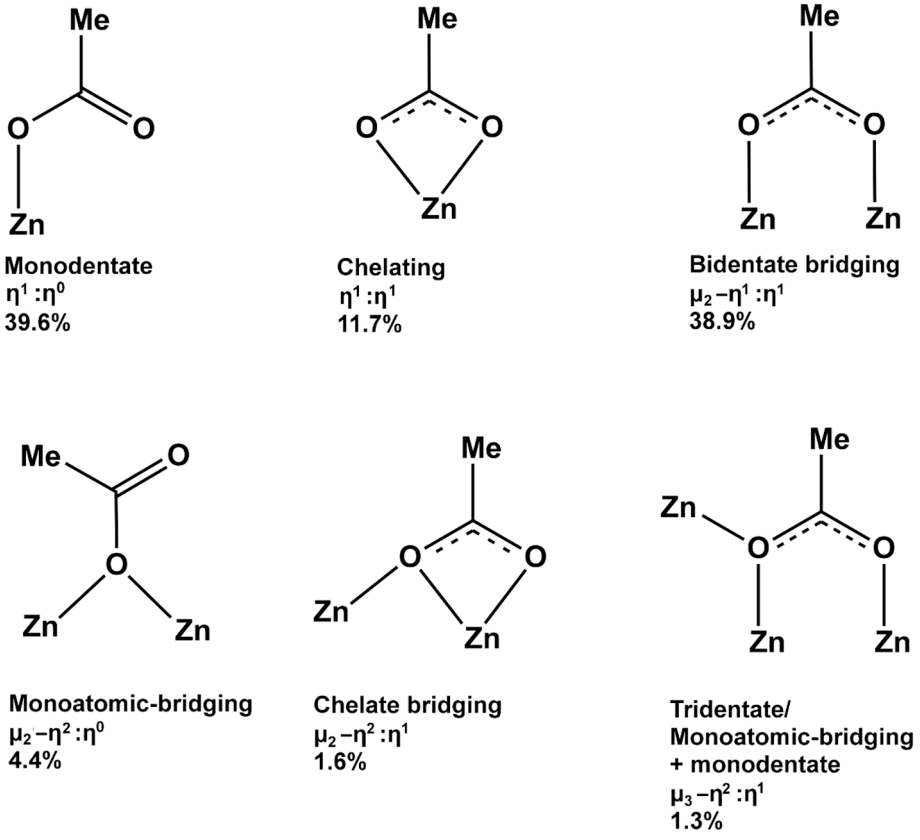

Scheme 2. A CSD analysis of coordination modes of acetate anion in complexes containing only Zn(II) as the central metal ion.

ligands. A detailed analysis of intermolecular interactions and density functional theory (DFT) and time-dependent DFT (TD-DFT) studies were also performed to ensure a comprehensive understanding.

2. Experimental

2.1. Materials and methods

Details regarding materials and methods are given in ESI (Section 2.1).

2.2. Synthesis of $[Zn_5(LS^1)_4(AcO)_6]$ (1-AcO) and $[Zn(LS^3)(AcO)(H_2O)]$ (3-AcO)

1-AcO: To a yellow solution of HLS^1 (0.1 g, 0.36 mmol) in THF (3 ml), a solution of $Zn(AcO)_2{\cdot}2H_2O$ (0.066 g, 0.45 mmol) in MeOH (0.5 ml) was added. After 15 min of reflux, an orange precipitate was formed. However, the reaction was continued under the same conditions for up to 2 h. The reaction mixture was cooled to RT, and the precipitate was filtered off and washed with THF. Single crystals of **1-AcO** were obtained by diffusion of hexane vapor into the MeOH solution of the crude precipitate. Yield: 0.096 g (60 %). Anal. Calcd for $C_{72}H_{62}N_{16}O_{12}S_4Zn_5$ (%): C, 48.08; H, 3.47; N, 12.46; S, 7.13. Found: C, 48.14; H, 3.82; N, 12.42; S, 7.46. IR (ATR, ν_{max}/cm^{-1}): 3102 (w), 3056 (w), 3003 (w), 2928 (w), 1593 (vs), 1548 (s), 1478 (ms), 1417 (vs), 1396 (vs), 1328 (vs), 1243 (vs), 1220 (s), 1157 (ms), 1096 (s), 941 (m), 891 (ms), 867 (m), 768 (m), 742 (m), 715 (w), 687 (m), 663 (m), 616 (m), 544 (w), 523 (w), 475 (vw). λ_M ($1{\cdot}10^{-3}$ M, DMSO) = 8.65 Ω^{-1} cm^2 mol^{-1}. NMR spectral data are given in ESI (Section 2.2).

3-AcO: To a yellow solution of HLS^3 (0.1 g, 0.36 mmol) in THF (10 ml), a solution of $Zn(AcO)_2{\cdot}2H_2O$ (0.066 g, 0.45 mmol) in MeOH (1 ml) was added, and the color of the mixture turned to red. The solution was refluxed for 30 min. Single crystals of **3-AcO** were obtained by diffusion of hexane vapor into the mother liquor cooled down to RT. Yield: 0.103 g (70 %). Anal. Calcd. for $C_{18}H_{18}N_4O_3SZn$ (%): C, 49.61; H, 4.16; N, 12.86; S, 7.36. Found: C, 49.35; H, 4.23; N, 12.87; S, 7.610. IR(ATR, ν_{max}/cm^{-1}): 2914 (m), 1597 (vs), 1551 (s), 1483 (ms), 1437 (vs), X (vs), 1352 (ms), 1320 (ms), 1266 (ms), 1241 (ms), 1184 (m), 1120 (ms), 1093 (m), 1021 (w), 935 (vw), 893 (m), 842 (w), 813 (w), 766 (w), 739 (w), 719 (vw), 676 (vw), 599 (vw), 515 (vw), 495 (vw). λ_M ($1{\cdot}10^{-3}$ M, DMSO) = 7.73 Ω^{-1} cm^2 mol^{-1}. NMR spectral data are given in ESI (Section 2.2).

Note: We have also tried to obtain and characterize the Zn(II) complex with HLS^2 by the reaction of the ligand and $Zn(AcO)_2{\cdot}2H_2O$ under the same experimental conditions as in the case of **1-AcO** and **3-AcO**. However, the attempt was unsuccessful. The obtained microcrystalline precipitate was not soluble in any conventional polar or non-polar solvent, even at elevated temperatures. Consequently, we were unable to obtain single crystals. IR (ATR, ν_{max}/cm^{-1}): 3115 (ms), 2840 (m), 1602 (vs), 1555 (s), 1498 (ms), 1432 (vs), 1410 (vs), 1329(s), 1247 (vs), 1177 (m), 1124 (ms), 1099 (m), 1028 (m), 897 (w), 827 (w), 775 (w), 739 (vw), 680 (w), 635 (w), 518 (vw).

2.3. NMR spectroscopy, X-ray crystallography, computational study, termal analysis and photophysical measurements

Experimental data for NMR spectroscopy, single crystal and powder X-ray diffraction (XRD) analysis, Hirshfeld surface analysis, electrostatic potential mapping, energy distribution of intermolecular interactions, termal analysis, photophysical measurements and details regarding DFT and TD-DFT calculation are given in ESI (Sections 2.2–2.9).

3. Results and discussion

3.1. General

The syntheses of the complexes were performed by refluxing reaction mixtures containing the ligands' solutions in THF with $Zn(AcO)_2$ solution in MeOH. After 1 h of refluxing, precipitates were obtained in the case of HLS^{1-2}, while there was no precipitation in the case of HLS^3. Single crystals of **1-AcO**, suitable for XRD analysis, were obtained by diffusion of hexane vapor into the MeOH solution of the crude precipitate. Because of its insolubility, it was impossible to characterize and recrystallize the microcrystalline product obtained in the reaction of HLS^2 and $Zn(AcO)_2$ in the THF/MeOH mixture. Single crystals of **3-AcO** were obtained by diffusion of hexane into the mother liquor. The composition of **1-AcO** and **3-AcO** was determined by elemental analysis. Both complexes are non-electrolytes. Structural characterization of the complexes in the solid state was performed using IR spectroscopy and single-crystal XRD, while the solution behavior was studied using NMR spectroscopy.

The IR spectra of the complexes were analyzed and compared with the IR spectra of the corresponding ligands. In the IR spectra of both complexes, there are characteristic bands that indicate the presence of coordinated acetate anions (**1-AcO**: 1598 and 1420 cm^{-1}; **3-AcO**: 1597 and 1438 cm^{-1}). In the IR spectrum of **1-AcO**, there are no bands in the region around 3000 cm^{-1}, which indicates the coordination of HLS^1 in its anionic form. In addition, the absence of the bands in this region indicates that **1-AcO** crystallizes without solvent molecules in the crystal structure. In contrast, the presence of a broad, strong band in the IR spectrum of **3-AcO** in the region around 3000 cm^{-1} indicates the formation of hydrogen interactions due to the presence of coordinated acetate anion and a water molecule. In the IR spectra of the ligands, there are bands at ~1600 and ~1570 cm^{-1}, which can be assigned to the ν(C═N) of the azomethine group and thiazole ring, respectively [2]. In the spectra of the complexes, these bands are significantly shifted to lower frequencies (~1475 and 1400 cm^{-1}, respectively), which indicates coordination *via* these nitrogen atoms [6,42].

Based on the analysis of NMR spectra of both complexes (ESI, Section 3.1) and comparison with the spectra of the corresponding free ligands, it can be concluded that $HLS^{1,3}$ ligands are coordinated in the deprotonated form to Zn(II). The deprotonation of the ligands leads to an upfield shift of all signals in the ^1H NMR spectra of the complexes. This is in agreement with the data obtained for **1** containing deprotonated HLS^1 [6]. However, NMR analysis revealed the presence of two signal sets in ^1H and ^{13}C spectra of **1-AcO** and **3-AcO**. The existence of two complex species in DMSO solution of **1-AcO** and **3-AcO** can be attributed to the labile nature of both Zn(II) (due to d^{10} electronic configuration) and acetate ligands, thus making these complexes highly dinamic in solution at ambient temperature. Nevertheless, the conductivity measurements, performed at room temperature (RT) in DMSO solutions of the complexes during 24 h, coupled with NMR spectroscopy data, indicate that both complex species that exist in DMSO solution of **1-AcO** and **3-AcO** are non-electrolytes, *i.e.,* neutral complex species. A detailed discussion of NMR spectroscopy data is given in ESI (Section 3.1).

3.2. Molecular structures

Crystallographic data and refinement parameters for **1-AcO** and **3-AcO** are presented in Table S3 (ESI, Section 3.2). ORTEP drawings of the complexes are depicted in Fig. 1. Selected bond distances and angles are given in Tables S4 and S5 (ESI, Section 3.2). Pentanuclear complex **1-AcO**, $[Zn_5(LS^1)_4(AcO)_6]$, crystallizes in a monoclinic $P2_1/n$ space group, with half of the molecule in the asymmetric unit. Its structure is based on a central $Zn_3(AcO)_6$ cluster and two mononuclear zinc units with internal and terminal meridionally placed $(LS^1)^-$ ligands. In the distorted octahedral mononuclear units, both ligands are coordinated to Zn1 tridentately *via* $N_{py}N_{im}N_{th}$ nitrogen donor atoms. However, N3 hydrazone

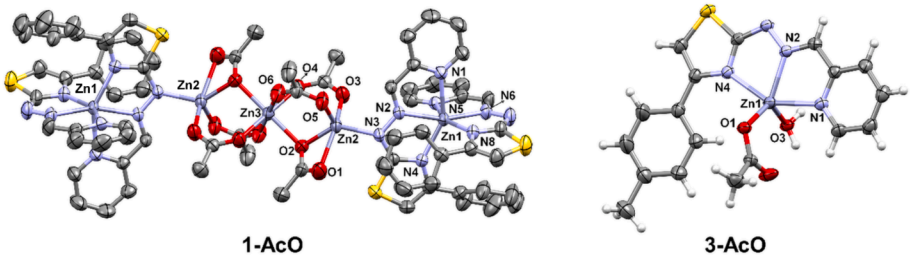

Fig. 1. ORTEP drawings of the molecular structures of **1-AcO** (left) and **3-AcO** (right). Thermal ellipsoids are given at the 30% probability level. Hydrogen atoms in the structure of **1-AcO** are omitted for clarity, while in the structure of **3-AcO**, they are drawn as spheres of arbitrary radii. Zn3 atom of **1-AcO** lies at the inversion center at 1, ½, 0.

nitrogen atoms from internal $(LS^1)^-$ ligands connect mononuclear units to the central $Zn_3(AcO)_6$ cluster by Zn2–N3 bonds. Thus, the coordination mode of the internal ligand can be described as tridentate-bridging. The atom Zn3 from the central cluster lies at the inversion center (site symmetry: 1, ½, 0; Wyckoff letter *c*). It is coordinated with six acetate anions. The geometry around Zn3 is almost regular octahedral. In contrast, Zn2 ions from the cluster are coordinated to three acetate ions. Two acetate ions connect Zn2 and Zn3 through a bidentate bridging mode (μ_2–η^1:η^1), while one acetate ion is coordinated to Zn2 *via* a chelate bridging mode (μ_2–η^2:η^1). The geometry around Zn2 is distorted square-pyramidal with the geometric index of distortion

$\tau_5 = 0.33$ (0.00 for square pyramidal and 1.00 for trigonal bipyramidal) [43]. CSD survey indicates that **1-AcO** is the first complex with PTHs in which the N_{hyd} nitrogen atom is coordinated to a central metal ion [14]. In addition, it is the first complex with both classes of PTH ligands, which is not mononuclear or polymer but pentanuclear [14]. There are 17 structures containing $Zn_3(AcO)_6$ clusters deposited in the CSD. Clusters in these structures can be classified into four types according to the coordination modes of acetate ions (Table S6, ESI). Observed 4(μ_2–η^1:η^1)/2(μ_2–η^2:η^1) acetate coordination found in the **1-AcO** cluster unit seems to be unique in that respect.

Complex **3-AcO** crystallizes in a triclinic *P*–1 space group with one molecule in the asymmetric unit. One $(LS^3)^-$ ligand is $N_{py}N_{im}N_{th}$ tridentately coordinated to Zn(II) ion. The pentacoordination is completed by the oxygen atoms from one water molecule and acetate anion. Therefore, a neutral molecular complex is formed. The zinc atom is embedded in a coordination sphere that can be described as significantly distorted square-pyramidal, with the τ value of 0.45 [43].

3.3. Mechanism of *1-AcO* formation

The proposed mechanism of **1-AcO** formation is based on the point zero charge model by Raman and Whittingham [44]. According to this model, when a metal salt is dissolved in water or a non-aqueous solvent, neutral solute complexes are formed, and such complexes further undergo a condensation reaction at the isoelectric point. The way condensation occurs depends on the nature of the metal salt, the added organic ligands, the polarity of the solvent, the pH value of the environment, and the stoichiometry of the reactants. Based on this mechanism, Kumar et al. further proposed a mechanism for forming Zn(II) trinuclear complexes with various lutidines containing clusters similar to **1-AcO** [45]. The proposed mechanism of **1-AcO** formation is shown in Scheme 3. In the first step, the reaction between HLS^1 and Zn $(AcO)_2{\cdot}2H_2O$ in a THF/MeOH mixture produces a neutral complex X, where the acetate anion acts as a base and deprotonates the hydrazone nitrogen atom of HLS^1 ligand. This is consistent with the point zero charge model. It is known that in an aqueous solution of $Zn(AcO)_2$, various acetate species are formed, such as $[Zn(AcO)_n]_{2-n}$ ($n = 1, 2$) [46–49]. Quantum mechanical calculations showed that in an ethanol solution, both tetrahedral $[Zn(AcO)_2(EtOH)]$ and octahedral $[Zn(AcO)_2(EtOH)_2]$ species can exist [50]. Therefore, one or more neutral species, such as Y and Z, could simultaneously exist in the MeOH/THF solution (Scheme 3). In the second step, a condensation reaction between the formed neutral complex X and species Y and Z could occur in the sequence XYXYX, during which the pentanuclear complex **1-AcO** is formed (Scheme 3).

3.4. Crystal packing analysis

The presence of different types of intermolecular interactions in the crystal packings of **1-AcO** and **3-AcO** were first analyzed using a conventional crystallographic atom•••atom based approach (Table S7, ESI).

The crystal packing of both complexes is mainly based on hydrogen and π•••π stacking interactions. In the crystal structure of **1-AcO**, three structural motifs (motifs 1–3, Fig. 2A) can be identified. Intermolecular interactions in motif 1 comprise non-classical hydrogen C—H•••X interactions with sulfur and nitrogen atoms as acceptors, while in motifs 2 and 3, C—H•••O, C—H•••π and π•••π stacking interactions are present (Fig. 2A; Table S7, ESI). Interactions in motif 1 are responsible for the formation of 1D chains. These chains are interconnected into 2D layers parallel to (0 0 1) crystallographic plane by the interactions in motif 2 (Fig. S9A, ESI). Finally, 2D layers are further connected into the 3D supramolecular structure through interactions present in motif 3 (Fig. S9B, ESI). The crystal packing of **3-AcO** is based on (non-)classical hydrogen and π•••π stacking interactions displayed by motifs 1–4 (Fig. 3A). Intermolecular interactions present in motifs 1 and 3 are classical hydrogen O—H•••N/O interactions, where the oxygen atom of the coordinated water molecule (O3) is a double donor, and the deprotonated hydrazone nitrogen atom (N3) and the oxygen atom of the coordinated acetate anion (O2) are acceptors (Fig. 3A; Table S7, ESI). In motif 2, the molecules are connected *via* non-classical hydrogen interactions C—H•••O and π···π stacking interactions between pyridine and thiazole rings (Fig. 3A; Table S7, ESI). In motif 4, there are π···π interactions between benzene rings, as well as C—H•••π interactions between the same benzene ring and one of the methyl hydrogen atoms of the ligand (Fig. 3A; Table S7, ESI). The overall crystal packing of **3-AcO** can be described in terms of the formation of 1D chains parallel to the *a*-crystallographic axis by the interactions of motifs 1 and 2. These chains are connected *via* motif 3 into 2D layers parallel to (0 0 1) crystallographic plane (Fig. S10A, ESI). 2D layers are interconnected into 3D supramolecular structure *via* interactions present in motif 4 (Fig. S10B, ESI).

A whole-of-molecule approach was applied to understand intermolecular interactions and gain a fuller appreciation of the important interactions in the crystal structures of **1-AcO** and **3-AcO**. For this purpose, Hirshfeld surface analysis was carried out [51–53]. The distances d_{norm} were mapped on the Hirshfeld surfaces of **1-AcO** and **3-AcO**, providing a 3D picture of intermolecular close contacts (Fig. S11, ESI). Close contacts are also summarized in 2D pseudosymmetric fingerprint plots (Fig. S11, ESI). Relative contributions to the Hirshfeld surface of each type of intermolecular contact, excluding H•••H contacts, are shown in Table 2. In both complexes, relative contributions of close contacts follow the same trend: C···H>O···H>S···H>N···H>C···C (Table 2). The

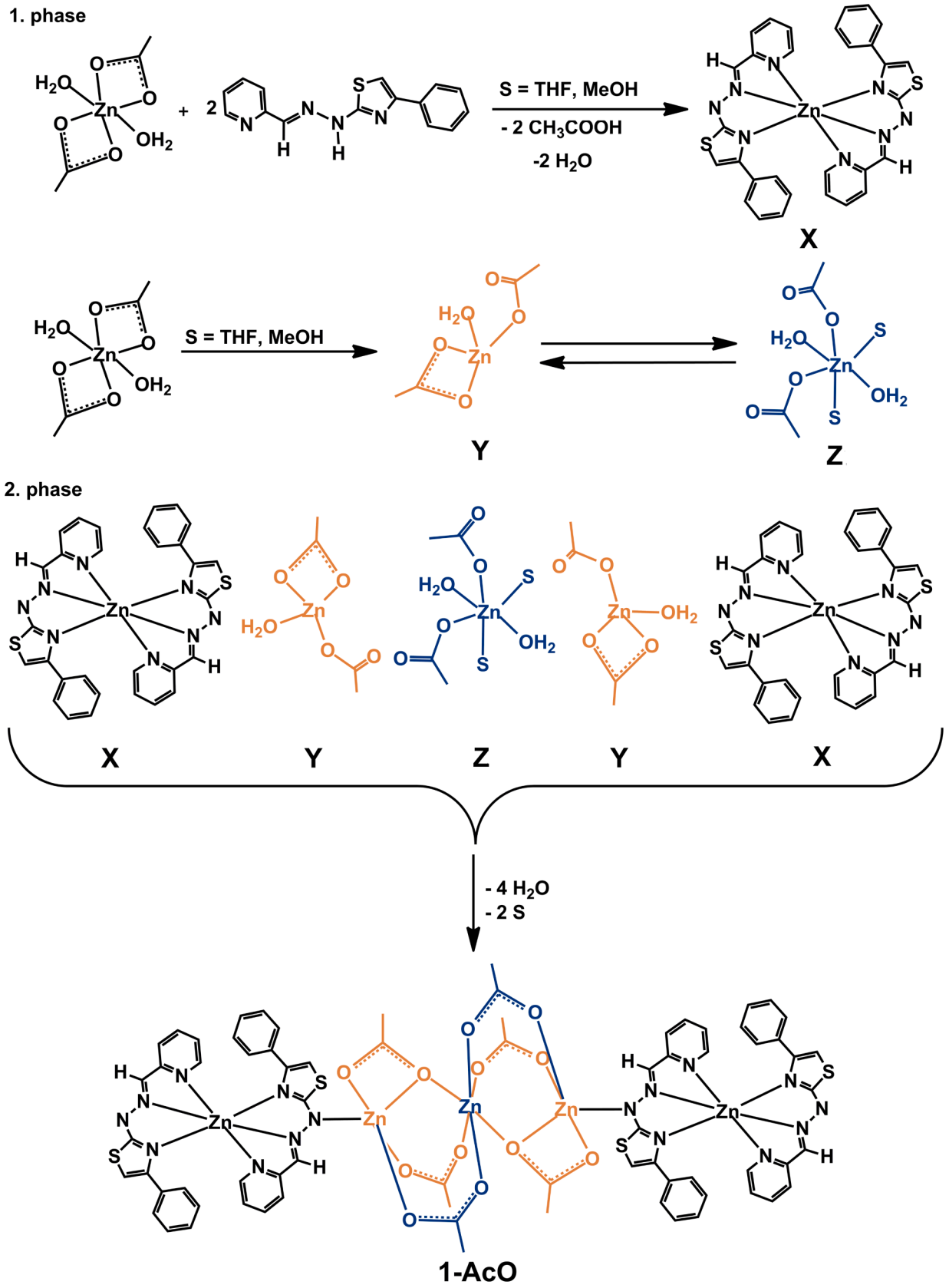

Scheme 3. The assumed mechanism of formation of pentanuclear complex **1-AcO**.

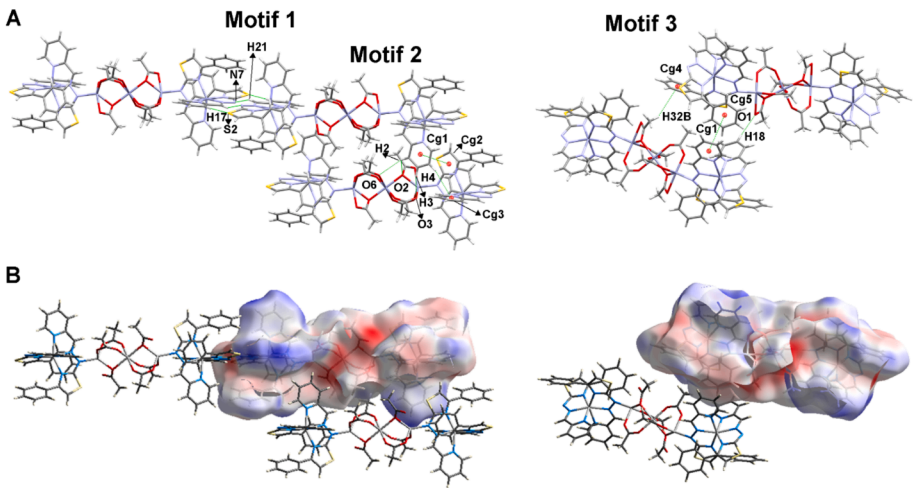

Fig. 2. (**A**) Motifs 1–3 in the crystal packing of **1-AcO** showing hydrogen and π•••π stacking interactions. (**B**) EPS mapped on the Hirshfeld surface of the central **1-AcO** molecule, showing intermolecular interaction with neighboring molecules.

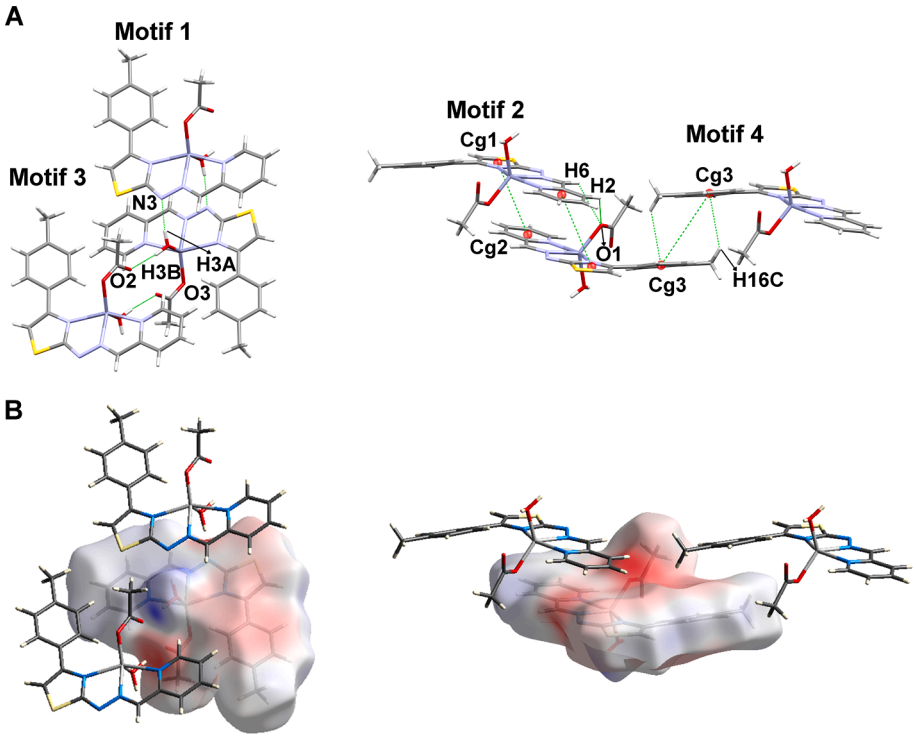

Fig. 3. (**A**) Motifs 1–4 in the crystal packing of **3-AcO** showing (non-)classical hydrogen and π•••π stacking interactions. (**B**) EPS maps mapped on the Hirshfeld surface of the central **3-AcO** molecule showing intermolecular interaction with neighboring molecules.

Table 2
Relative contributions to the Hirshfeld surface of selected types of intermolecular contacts (in %).

Intermolecular contact type		H•••C	H•••N	H•••S	C•••C	O•••H
1-AcO	Relative contribution to the Hirshfeld surface (%)	20.8	5.0	6.8	2.2	8.9
3-AcO		15.9	6.4	8.2	4.0	9.4

most intensive red patches on the surface colored according to d_{norm} are related to the N···H and O···H contacts (Fig. S11, ESI). The Hirshfeld surface breakdown into specific atom/atom type contacts reveals that 5.0 % and 8.9 % of the surface for **1-AcO** can be identified as N···H and O···H contacts, respectively, realized through mentioned C—H•••N/O interactions in the motifs 1–3. On the other hand, for **3-AcO**, 6.4 % and 9.4 % of the surface can be identified as N···H and O···H contacts, respectively, realized through mentioned classical hydrogen O—H•••N/O interactions in motifs 1 and 3, as well as non-classical hydrogen C—H•••O interaction in motif 2. Although S···H contacts have a greater contribution to the surface (6.8 % and 8.2 % in **1-AcO** and **3-AcO**, respectively) than N···H contacts, the former represents the longer

contacts and can be seen as a white patch on d_{norm} Hirshfeld surface (Fig. S11, ESI).

Electrostatic potential (ESP) maps, calculated for the complexes, were mapped onto the Hirshfeld surface of the complexes (Fig. S12, ESI) since the mentioned close contacts can also be explained in terms of the electrostatic complementarity of touching surface patches of neighboring molecules. This enables a deeper insight into the nature of intermolecular interactions. The ESP map of **1-AcO** reveals the electropositive (blue) regions surrounding imine hydrogen atom (H21) and pyridine hydrogen atoms (H2, H3, H4, and H18), while electronegative (red) regions are situated around the deprotonated hydrazone nitrogen atom (N7) and coordinated oxygen atoms (O1, O2, O3 and O6) from acetate ions (motif 1–3, Fig. 2B). A part of the Hirshfeld surface has strongly electronegative potential (–0.0946 au) over the oxygen atom O1 from the acetate ion coordinated in chelate bridging mode, while C18–H18 from pyridine ring lays in the region of positive potential (0.0564 au) resulting in the formation of motif 3 (Fig. 2B). In **3-AcO**, regions with the largest negative electrostatic potential are located around the non-coordinated acetate oxygen atom O2 and deprotonated hydrazone nitrogen atom N3. A part of the Hirshfeld surface is strongly electropositive over the hydrogen atoms H3A and H3B from the coordinated water molecule (Fig. 3B). Also, the ESP map reveals that the thiazole ring has electronegative potential, while the surface above the pyridine ring is electropositive, which indicates significant π···π stacking interactions in **3-AcO** (Fig. 3B). An angle between the least-square plane through atoms of tolyl moiety and the least-square plane through atoms of the rest of the coordinated ligand molecule is 19° in **3-AcO** (Fig. S13, ESI); thus, the ligand $(LS^3)^-$ is almost planar. The coordination of one $(LS^3)^-$ ligand and its planarity facilitate π···π stacking interactions between adjacent complex molecules.

3.5. Intermolecular interaction energies and energy frameworks

Intermolecular interaction energies obtained by the single-point energy calculations in the crystal structure of **3-AcO** are given in Table S8 (ESI), but the same methodology cannot be applied to the **1-AcO** due to the size of the molecular structure (171 atoms). Next, we applied a whole-of-molecule approach to understanding the energies of intermolecular interactions in crystal packing of **1-AcO** and **3-AcO**. This avoids focusing on specific atom–atom interactions and visualizes energies as an energy framework [54]. Values of the total energy of interactions for pairs of neighboring molecules were calculated, whereby the total energies are broken down into components: electrostatic, dispersive, polarization, and repulsion (Table S9, ESI). The topology of intermolecular interactions in the crystal packings of **1-AcO** and **3-AcO** is revealed by representing the network of nearest neighbor energies by a framework of cylinders whose width is proportional to the strength of the interaction(s). Separate frameworks for the electrostatic and dispersion components provide insight into the nature of different interactions. In the crystal packing of **1-AcO**, a dispersion has the largest contribution to the intermolecular interaction energy, followed by the electrostatic energy component in all pairs of the neighboring molecules (Fig. 4A and B; Table S9, ESI). The crystal packing of **1-AcO** is mainly stabilized by the formation of non-classical hydrogen and π●●●π stacking interactions, which are primarily dispersive in origin. The stabilizing energies are strongest between molecular pars along the *a*-crystallographic axis (Fig. 4A). In the crystal structure of **3-AcO**, dispersion is the main component of energy interactions between the largest number of neighboring molecules (Fig. 4C; Table S9, ESI). Nevertheless, the electrostatic component has the greatest contribution to the total energy in two molecular pairs (motif 1 and 3, *vide supra*) that extend along the *b*-crystallographic axis (Fig. 4D; Table S9, ESI). This is rational considering that the classical hydrogen interactions are realized between molecules that are in close proximity in the crystal structure of **3-AcO**, while these interactions are absent in the crystal structure of **1-AcO**. The difference in the values of electrostatic interaction energies for **1-AcO** and **3-AcO** is due to the presence of a coordinated water molecule in the latter, leading to the formation of described classical hydrogen interactions.

3.6. PXRD analysis

Before the thermal and photophysical study, a phase analysis was performed to determine the phase purity of the synthesized complexes. PXRD analysis was performed on pulverized single-crystal samples of **1-**

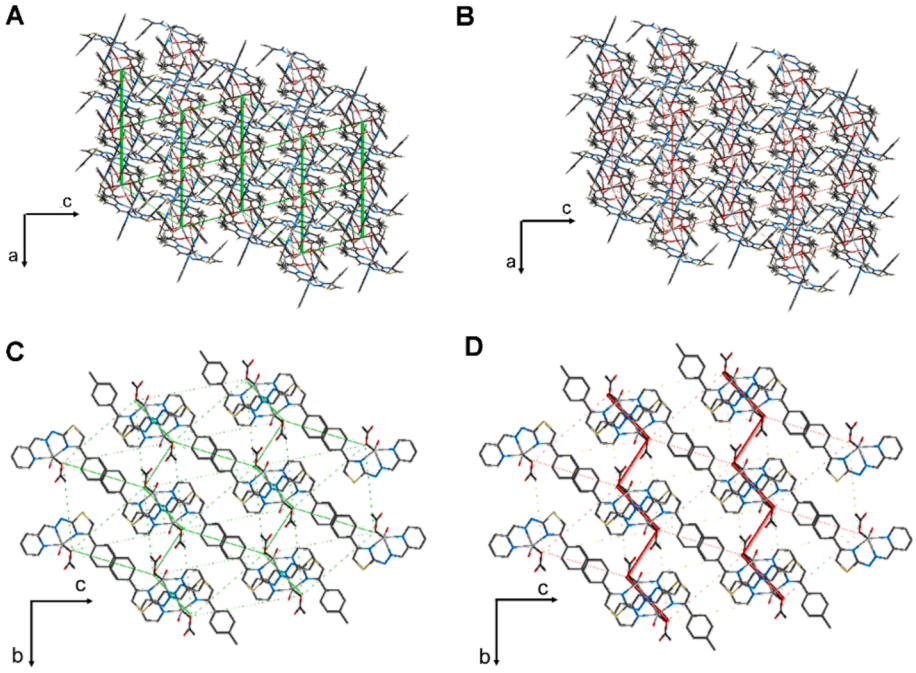

Fig. 4. Energy framework diagrams of dispersion (A) and electrostatic (B) energies for supercells (2 × 2 × 2) of **1-AcO** and dispersion (C) and electrostatic (D) energies for supercells (2 × 2 × 2) of **3-AcO**. All diagrams show cylinders of the same scale (green cylinders represent dispersion energy, and red cylinders represent electrostatic energy). (Colour online.)

AcO and **3-AcO**, while refinement was done using the Rietveld method using structural models obtained from the single-crystal XRD data. Based on the refinement, both complexes represent single-phase systems. Experimental and theoretically obtained powder X-ray diffractograms of **1-AcO** and **3-AcO** bulk samples overlap well (Fig. S14, ESI). The absence of other phases indicates that the single crystals of **1-AcO** and **3-AcO** are stable in the air under standard conditions and during grinding.

3.7. Thermal properties

1-AcO and **3-AcO** were analyzed by simultaneous thermogravimetry–differential scanning calorimetry in the air. **1-AcO** does not contain lattice or coordinated solvent molecules and it is stable up to ~300 °C. **3-AcO** loses the coordinated water molecule below 200 °C, but its dehydrated form decompose at ~300 °C. The measurements were carried out in argon, too. Up to ~400 °C, there are no significant differences between the decomposition of the complexes in an inert and oxidative atmosphere. The compounds were analyzed using online coupled TG-MS measurements in argon to examine the decomposition mechanism. A more detailed thermal analysis is provided in ESI (Section 3.3).

3.8. Photophysical and computational study of 3-AcO

The complex **1-AcO** does not display emissive properties, while the complex **3-AcO** exhibits luminescence in the solid state at RT and 77 K. Thus, it displays one emission at 610 nm (exc. 365–520 nm; $\Phi = 1.1$ %) with almost imperceptible shoulders that become more intense when the measurement is done at 77 K (Fig. 5A). These shoulders are likely to be related to a vibronic structure since the difference in energy between adjacent peaks is around 600–700 cm^{-1}. This energy range would correspond to C—S stretching vibrations that provokes a slight blue-shift of the emission band, although a rigidochromic effect would not be excluded. The featureless solid-state absorption spectrum for **3-AcO** (Fig. 5B) resembles that of the excitation one, which seems to indicate that the transitions responsible for the luminescence emission are allowed, indicating the existence of singlet–singlet transitions. As a confirmation, the lifetime measurement at RT lies in the nanosecond range (241 ns), together with the short Stokes' shift of ca. 2650 cm^{-1}. Accordingly, we can propose that the emissions arise from ligand-based transitions (*vide infra*). We recently reported a similar assignment on related Zn(II) complexes based on PTH ligands (Scheme 1) [5,6]. Also, the obtained results agree with our previous hypothesis since symmetric **1-AcO** is not photoluminescent, unlike asymmetrical **3-AcO**.

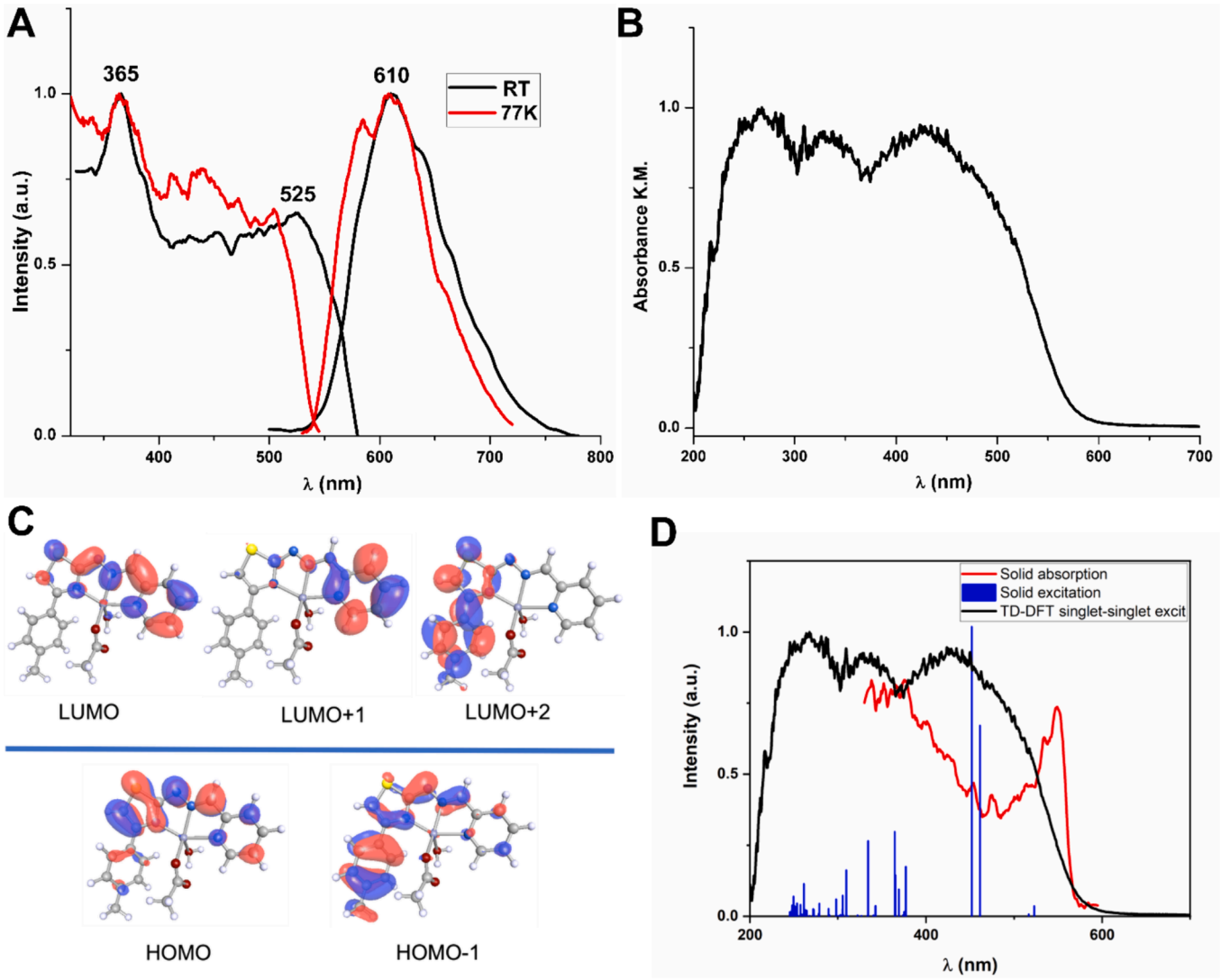

Fig. 5. Excitation and emission spectra for **3-AcO** at RT (black) and 77 K (red) in the solid state (A); solid-state absorbance spectrum of **3-AcO** (B); frontier molecular orbitals for model system **3-AcO-a** (C); and comparison between experimental absorption and excitation spectra with TD-DFT singlet–singlet excitations for model system **3-AcO** (D). (Colour online.)

Table 3
TD-DFT singlet–singlet excitation calculations for a model system of **3-AcO-a**.

Excitation	λ (nm)	Osc. strength	Contributions
$S_0 \rightarrow S_1$	479	0.376	112a → 113a (95) HOMO→LUMO (IL)
$S_0 \rightarrow S_2$	377	0.141	112a → 114a (83) HOMO→LUMO+1 (IL)
$S_0 \rightarrow S_4$	336	0.094	111a → 113a (84) HOMO-1 → LUMO (IL)
$S_0 \rightarrow S_{19}$	239	0.239	111a → 115a (72) HOMO-1 → LUMO+2 (IL)

These experimental results are supported by the analysis of the computed molecular orbitals and electronic singlet–singlet excitations obtained through DFT and TD-DFT calculations, respectively. First, we have fully optimized a model system **3-AcO-a** and compared the most important structural parameters with the molecular geometry obtained through single crystal XRD analysis for complex **3-AcO**. The computed results on the optimized molecular structure agree well with the experimental ones, showing similar distances, angles, and dihedral angles (Table S11, ESI). Following the optimized model **3-AcO-a** analysis, we have computed the frontier molecular orbitals (Fig. 5C). The most important characteristic of these MOs is that they are all located on the $(LS^3)^-$ ligand without the participation of the Zn(II) metal center or the O-donor acetate ligand. Therefore, it could be confirmed that the emissive properties displayed by the complex **3-AcO** would be related to intra-ligand (IL) transitions. To confirm the origin of the emissive properties of the complex **3-AcO**, we computationally reproduced the complex absorption spectrum through time-dependent DFT calculations (TD-DFT) of the first 40 singlet–singlet excitations for model **3-AcO-a**. Fig. 5D compares the experimental absorption and excitation spectra for **3-AcO** with the computationally predicted one. The predicted electronic excitations match the experimental spectra. A deeper analysis of these transitions is shown in Table 3. As can be observed, the transitions displaying larger oscillator strengths involve MOs located in the $(LS^3)^-$ ligand, and these MOs are shown in Fig. 5C. These results confirm the previous assignment of the emissions experimentally observed for this complex, in which a vibronic structure arising from C—S stretching vibrations within this ligand was proposed. Indeed, the C—S bonds participate in most of the MOs involved in the intense singlet–singlet excitations.

4. Conclusion

The synthesis and characterization of the first acetate-based zinc complexes with two PTHs ligands (HLS^1 and HLS^3), that differ in one methyl group, is reported. Under the same reaction conditions, the similar ligands form complexes of quite different structures, with general formulas $[Zn_5(LS^1)_4(AcO)_6]$ (**1-AcO**) and $[Zn(LS^3)(AcO)(H_2O)]$ (**3-AcO**). The structure of **1-AcO** is unique in several aspects. Namely, it is the first example of a pentanuclear complex based on a PTH ligand. It contains an unprecedented $Zn_3(AcO)_6$ cluster with four acetates coordinated in μ_2–η^1:η^1 mode and two acetates coordinated in μ_2–η^2:η^1 mode. Also, **1-AcO** represents the first example of a *d*-metal complex containing *NNNN* tetradentately coordinated PTH class I ligand. The formation of pentanuclear complex **1-AcO** may be explained by the point zero charge model, indicating the formation of several neutral complex species undergoing a condensation reaction. A similar sequence of reactions does not occur with HLS^3, probably due to steric repulsion caused by the presence of an additional methyl group. Consequently, **3-AcO** is a mononuclear complex with one $(LS^3)^-$ ligand *NNN* tridentately coordinated to the Zn(II) ion. The pentacoordination is completed by the oxygen atoms from one water molecule and acetate anion.

In our previous research, we proposed a hypothesis regarding the impact of symmetry on the quenching of the photophysical properties of Zn(II) complexes [5,6]. Our experimental results revealed that the photophysical properties of several Zn(II) complexes in the solid state, where the Zn(II) ion lies on a symmetry element, only exist if the ligands already exhibit photophysical properties. In this study, we examined the solid-state photophysical properties of **1-AcO**, pentanuclear centrosymmetric complex, and the asymmetrical **3-AcO**. Once again, our experimental results confirmed our hypothesis. TD-DFT studies suggested that the emissive properties of **3-AcO** stem from IL transitions, similar to its trigonal–bipyramidal analog **1-Cl**. Our study highlights the significance of molecular symmetry in predicting potential photoluminescence for Zn(II) complexes containing photo-inactive ligands. Nevertheless, it is essential to consider that various factors, such as ligand conformation, the geometry around the Zn(II) ion, intermolecular interactions, and the presence of solvent molecules, can also influence the electronic structure and thus the photophysical behavior of this class of complexes. In summary, this study supports our previously proposed hypothesis and motivates us to further investigate this phenomenon in greater detail, potentially including other metals besides Zn.

CRediT authorship contribution statement

Jovana B. Araškov: Writing – original draft, Investigation. **Alfonso T. Garcia-Sosa:** Writing – review & editing. **Aleksandar Višnjevac:** Investigation. **Sérgio F. Sousa:** Methodology. **Berta Barta Holló:** Investigation. **Özlem Uğuz:** Investigation. **Atıf Koca:** Validation. **Miguel Monge:** Investigation. **María Rodríguez-Castillo:** Investigation. **José M. López-de-Luzuriaga:** Writing – original draft. **Tamara R. Todorović:** Writing – review & editing. **Nenad R. Filipović:** Conceptualization, Writing – review & editing.

Declaration of competing interest

The authors declare that they have no known competing financial interests or personal relationships that could have appeared to influence the work reported in this paper.

Data availability

Data will be made available on request.

Acknowledgements

The authors acknowledge the financial support of the Ministry of Science, Technological Development and Innovations of the Republic of Serbia (Contract No's. 451-03-66/2024-03/200168, 451-03-65/2024-03/200116, 451-03-66/2024-03/200168 & 451-03-65/2024-03/200125). We thank the Turkish Academy of Sciences (TÜBA) for the financial support. J.M.L.L, M.M. M.R.C. thank Grant DGI MICINN/FEDER, project number PID2022-139739NB-I00 (AEI/FEDER, UE) and by "ERDF A way of making Europe". S.F.S. thanks the national funds from the Portuguese Foundation for Science and Technology (FCT) under the scope of the strategic funding UIDP/04378/2020 and UIDB/04378/2020. S.F.S. acknowledges FCT by funding 2020.01423.CEECIND/CP1596/CT0003. Some of the calculations were produced with the support of the INCD funded by the FCT and FEDER under project 01/SAICT/2016 number 022153, and projects CPCA/A00/7140/2020 and CPCA/A00/7145/2020.

Appendix A. Supplementary data

CCDC 2350808 and 2350809 contain the supplementary crystallographic data for **1-AcO** and **3-AcO**. These data can be obtained free of charge *via* https://www.ccdc.cam.ac.uk/conts/retrieving.html or from the Cambridge Crystallographic Data Centre, 12 Union Road, CambridgeCB2 1EZ, UK; fax: (+44) 1223-336-033; or e-mail: deposit@ccdc.cam.ac.uk. Supplementary data to this article can be found online at https://doi.org/10.1016/j.poly.2024.117162.

References

[1] N.R. Filipović, H. Elshaflu, S. Grubišić, L.S. Jovanović, M. Rodić, I. Novaković, A. Malešević, I.S. Djordjević, H. Li, N. Šojić, A. Marinković, T.R. Todorović, Dalt. Trans. 46 (2017) 2910.
[2] H. Elshaflu, S. Bjelogrlić, C.D. Muller, T.R. Todorović, M. Rodić, A. Marinković, N. R. Filipović, J. Coord. Chem. 69 (2016) 3354–3366.
[3] S.B. Marković, A.V. Natalia Maciejewska, M. Olszewski, A. Puerta, J.M. Padrón, I. Novaković, S. Kojić, H.S. Fernandes, S.F. Sousa, S. Ramotowska, A. Chylewska, M. Makowski, T.R. Todorović, N.R. Filipović, Eur. J. Med. Chem. 238 (2022) 11449.
[4] S.B. Kokanov, N.R. Filipović, A. Višnjevac, M. Nikolić, I. Novaković, G. Janjić, B. B. Holló, S. Ramotowska, P. Nowicka, M. Makowski, Ö. Uğuz, A. Koca, T. R. Todorović, Appl. Organomet. Chem. (2022) 1–20.
[5] J. Araškov, A. Višnjevac, J. Popović, V. Blagojević, H.S. Fernandes, S. Sousa, I. Novakovic, J.M.M. Padrón, B. Hollo, M. Monge, M. Rodríguez-Castillo, J. M. López-de-Luzuriaga, N.R. Filipović, T.R. Todorović, CrystEngComm 24 (2022) 5194.
[6] J.B. Araškov, N. Maciejewska, M. Olszewski, A. Višnjevac, V. Blagojević, H. S. Fernandes, S.F. Sousa, A. Puerta, J.M. Padrón, B.B. Holló, M. Monge, M. Rodríguez-Castillo, J.M. López-de-Luzuriaga, Ö. Uğuz, A. Koca, T.R. Todorović, N.R. Filipović, J. Mol. Struct. 1281 (2023) 135157.
[7] P. Bera, P. Brandão, G. Mondal, H. Jana, A. Jana, A. Santra, P. Bera, Polyhedron 134 (2017) 230–237.
[8] P. Bera, A. Aher, P. Brandao, S.K. Manna, I. Bhattacharyya, C. Pramanik, B. Mandal, S. Das, P. Bera, J. Mol. Struct. 1224 (2021) 129015.
[9] P. Bera, A. Aher, P. Brandao, U. Debnath, V. Dewaker, S.K. Manna, A. Jana, C. Pramanik, B. Mandal, P. Bera, J. Chem. Inf. Model. 62 (2022) 1437–1457.
[10] X.Z. Zou, A.S. Feng, Y.Z. Liao, X.Y. Xu, H.Y. Wen, A. You, M. Mei, Y. Li, Inorg. Chem. Commun. 118 (2020) 1–5.
[11] X. Zou, P. Shi, A. Feng, M. Mei, Y. Li, Transit. Met. Chem. 46 (2021) 263–272.
[12] X. Zou, Y. Liao, C. Yang, A. Feng, X. Xu, H. Jiang, Y. Li, J. Coord. Chem. 74 (2021) 1009–1027.
[13] Z. Xun-Zhong, F. An-Sheng, Z. Fu-Ran, L. Min-Cheng, L. Yan-Zhi, M. Meng, L. Yu, Bioinorg. Chem. Appl. 2020 (2020) 1–9.
[14] C.R. Groom, I.J. Bruno, M.P. Lightfoot, S.C. Ward, Acta Crystallogr. Sect. B Struct. Sci. Cryst. Eng. Mater. 72 (2016) 171–179.
[15] M. Porchia, M. Pellei, F. Del Bello, C. Santini, Molecules 25 (2020) 5814.
[16] M. Pellei, F. Del Bello, M. Porchia, C. Santini, Coord. Chem. Rev. 445 (2021) 214088.
[17] K. Bajaj, R.M. Buchanan, C.A. Grapperhaus, J. Inorg. Biochem. 225 (2021) 111620.
[18] A. Majumder, C. Sarkar, I. Das, S. Sk, S. Bandyopadhyay, S. Mandal, M. Bera, ACS Appl. Mater. Interfaces 15 (2023) 22781–22804.
[19] Y. Zhang, X. Li, J. Li, M.Z.H. Khan, F. Ma, X. Liu, BMC Chem. 15 (2021) 1–12.
[20] T.S. Lobana, S. Indoria, H. Sood, D.S. Arora, M. Kaur, J.P. Jasinski, Dalt. Trans. 50 (2021) 6823–6833.
[21] S.N. Riduan, Y. Zhang, Chem. - an Asian J. 16 (2021) 2588–2595.
[22] X. Wang, S. He, L. Yuan, H. Deng, Z. Zhang, J. Agric. Food Chem. 69 (2021) 3952–3964.
[23] F. Marchetti, R. Pettinari, F. Verdicchio, A. Tombesi, S. Scuri, S. Xhafa, L. Olivieri, C. Pettinari, D. Choquesillo-Lazarte, A. García-García, A. Rodríguez-Diéguez, A. Galindo, Dalt. Trans. 51 (2022) 14165–14181.
[24] D. Sengupta, U. Timilsina, Z.H. Mazumder, A. Mukherjee, D. Ghimire, M. Markandey, K. Upadhyaya, D. Sharma, N. Mishra, T. Jha, S. Basu, R. Gaur, Eur. J. Med. Chem. 174 (2019) 66–75.
[25] D. Sengupta, M. Rai, Z. Hoque Mazumdar, D. Sharma, K. Malabika Singha, P. Pandey, R. Gaur, B. Med, Chem. Lett. 65 (2022) 128699.
[26] J. Kladnik, A. Dolinar, J. Kljun, D. Perea, J. Grau-Expósito, M. Genescà, M. Novinec, M.J. Buzon, I. Turel, J. Enzyme Inhib. Med. Chem. 37 (2022) 2158–2168.
[27] A.V. Teles, T.M.A. Oliveira, F.C. Bezerra, L. Alonso, A. Alonso, I.E. Borissevitch, P. J. Gonçalves, G.R.L. Souza, J. Gen. Virol. 99 (2018) 1301–1306.
[28] C.I. Chukwuma, S.S. Mashele, K.C. Eze, G.R. Matowane, S.M. Islam, S.L. Bonnet, A. E.M. Noreljaleel, L.M. Ramorobi, Pharmacol. Res. 155 (2020) 104744.
[29] N. Kumar, V.B. Roopa, M. Kumar, Coord. Chem. Rev. 427 (2021) 213550.
[30] J.M. Parr, M.R. Crimmin, Chem. Sci. 14 (2023) 11012–11021.
[31] P. de Frémont, N. Adet, J. Parmentier, X. Xu, B. Jacques, S. Dagorne, Coord. Chem. Rev. 469 (2022) 214647.
[32] M. Strianese, D. Pappalardo, M. Mazzeo, M. Lamberti, C. Pellecchia, Dalt. Trans. 49 (2020) 16533–16550.
[33] R. Diana, B. Panunzi, Molecules 26 (2021) 4176.
[34] T. Tsukamoto, K. Takada, R. Sakamoto, R. Matsuoka, R. Toyoda, H. Maeda, T. Yagi, M. Nishikawa, N. Shinjo, S. Amano, T. Iokawa, N. Ishibashi, T. Oi, K. Kanayama, R. Kinugawa, Y. Koda, T. Komura, S. Nakajima, R. Fukuyama, N. Fuse, M. Mizui, M. Miyasaki, Y. Yamashita, K. Yamada, W. Zhang, R. Han, W. Liu, T. Tsubomura, H. Nishihara, J. Am. Chem. Soc. 139 (2017) 5359–5366.
[35] C.B. Kc, G.N. Lim, F. D'Souza, Nanoscale 7 (2015) 6813–6826.
[36] G. Swart, E. Fourie, J.C. Swarts, Inorg. Chem. 61 (2022) 13306–13321.
[37] P. Pal, A. Datta, R. Jana, S. Malik, Eur. Polym. J. 194 (2023) 112115.
[38] M. Zhao, J.C. Jimenez, C. Wang, G. Rui, T. Ma, C. Lu, A.L. Rheingold, R. Li, L. Zhu, G. Sauvé, J. Phys. Chem. C 126 (2022) 6543–6555.
[39] A.A. Dar, A.A. Malik, J. Mater. Chem. C 12 (2024) 9888–9913.
[40] F. Dumur, Synthetic Met. 195 (2014) 241–251.
[41] G.U. Mahoro, J. Fernandez-Cestau, J.-L. Renaud, P.B. Coto, R.D. Costa, S. Gaillard, Adv. Opt. Mater. 8 (2020) 2000260.
[42] P. Bera, A. Aher, P. Brandao, S.K. Manna, I. Bhattacharyya, G. Mondal, A. Jana, A. Santra, P. Bera, New J. Chem. 45 (2021) 11999–12015.
[43] L. Yang, D.R. Powell, R.P. Houser, Dalt. Trans. (2007) 955–964.
[44] A. Ramanan, M.S. Whittingham, Cryst. Growth Des. 6 (2006) 2419–2421.
[45] U. Kumar, J. Thomas, N. Thirupathi, Inorg. Chem. 49 (2010) 62–72.
[46] D.A. Brown, L.P. Cuffe, N.J. Fitzpatrick, Á.T. Ryan, Inorg. Chem. 43 (2004) 297–302.
[47] R.S. Kolat, J.E. Powell, Inorg. Chem. 1 (1962) 293–296.
[48] J.E. Tackett, Appl. Spectrosc. 43 (1989) 483–489.
[49] S.J. Borg, W. Liu, Nucl. Instrum. Methods Phys. Res. Sect. A 619 (2010) 276–279.
[50] J. Reyna-Luna, R. Flores, R. Gómez-Balderas, M. Franco-Pérez, J. Phys. Chem. B 124 (2020) 3355–3370.
[51] J.M.A. Spackman, J.J. McKinnon, CrystEngComm. 4 (2002) 378–392.
[52] J. McKinnon, D. Jayatilaka, M. Spackman, Chem. Comm. (2007) 3814–3816.
[53] T. Maity, H. Mandal, A. Bauza, B.C. Samanta, A. Frontera, S.K. Seth, New J. Chem. 42 (2018) 10202–10213.
[54] C.F. Mackenzie, P.R. Spackman, D. Jayatilaka, M.A. Spackman, IUCrJ 4 (2017) 575–587.